Materials Characterization 189 (2022) 111953

Contents lists available at ScienceDirect

Materials Characterization

journal homepage: www.elsevier.com/locate/matchar

Characterising the high temperature tensile behaviour of laser powder bed fused duplex stainless steel 2205 using the small punch test

Spencer Jeffs [a,*], Rory Douglas [a], Will Beard [a], Mark Coleman [a], Jack Adams [b], Thomas Jones [b], Dave Poole [b], Robert Lancaster [a]

[a] Institute of Structural Materials, Faculty of Science and Engineering, Bay Campus, Swansea University, Swansea SA1 8EN, United Kingdom
[b] Rolls-Royce plc., Kings Place, 90 York Way, London N1 9FX, United Kingdom

ARTICLE INFO

Keywords:
Additive manufacturing
Laser powder bed fusion
Duplex stainless steel
Small punch testing
Microstructure
Heat treatment

ABSTRACT

Duplex stainless steels (DSS) are a family of stainless steel alloys that benefit from the presence of two relatively equally proportioned phases, ferrite and austenite. The alloys are designed to have an enhanced resistance to corrosion and superior strength properties in comparison to more common stainless steel alloys such as 316 L. Design engineers are now exploring the introduction of additively manufactured (AM) DSS into industrial components, to benefit from these enhanced capabilities provided by the alloy and the greater flexibility in design offered by AM. This research focuses on the mechanical and microstructural characterisation of DSS 2205, manufactured by the AM process laser powder bed fusion (LPBF). Results have been generated through both uniaxial tensile testing and small punch (SP) testing on as built and heat-treated conditions, across a range of temperatures up to 750 °C. Microstructural assessments have been conducted using advanced microscopy to determine relevant phase distributions and texture morphologies present in the materials, to understand how this influences mechanical performance.

1. Introduction

Duplex stainless steels (DSS) are characterised by their dual phase structure, consisting of face centred cubic (FCC) austenite and body centred cubic (BCC) ferrite. There is no formal definition for the volume fraction distribution between austenite/ferrite, although typically the lesser volume is at least 30%. The amount of each phase is dependent on chemical composition and heat treatment [1,2]. DSS can offer numerous advantages compared to austenitic stainless steels, including increased strength enabling weight savings through thinning similar components as well as enhanced resistance to stress corrosion cracking [2,3]. Due to this unique combination of properties, DSS has seen interest across a range of industries, including nuclear, chemical, and marine [4,5]. DSS 2205 (otherwise recognised as UNS S31803) is one of the most widely used DSS alloys and is the focus of this investigation. A key limitation of DSS alloys can be embrittlement occurring at elevated temperatures due to the precipitation of undesired phases, such as σ and χ [6].

Additive Manufacturing (AM) is a technique that offers numerous benefits such as lean manufacturing, and the potential to produce complex, structurally optimised, and near net- and net-shaped components, previously not possible using more traditional manufacturing methods. AM has seen extensive research and investigation across a range of metallic systems due to these advantages, where understanding the processing, microstructure, and property relationships is vital to exploit its full potential [7]. LBPF is a prominent AM technique that is often employed for the AM of steels. In the case of LBPF-steels it has been shown that generally they can be manufactured to almost full relative density. However, the as-built microstructure is dominated by solidification and solid-state phase transformations and post build heat treatments are often necessary to produce a desired final microstructure [8,9]. In the case of LPBF DSS, the high cooling rates seen after solidification typically lead to an entirely ferritic formation in the as-built condition, providing high strength with limited ductility. Therefore, the as-built structure is prone to cracking under residual stresses. Annealing heat treatments can be implemented to restore the dual phase microstructure, resulting in reduced strength but an increased ductility [9,10].

Considering the vast range of parameters that influence LBPF materials, such as powder feedstock characteristics, processing parameters, and post process treatments, to conduct a full mechanical test

* Corresponding author.
E-mail address: s.p.jeffs@swansea.ac.uk (S. Jeffs).

https://doi.org/10.1016/j.matchar.2022.111953
Received 28 January 2022; Received in revised form 4 May 2022; Accepted 6 May 2022
Available online 11 May 2022

programme to generate a holistic understanding of the mechanical properties would ultimately be a costly procedure. As such the Small Punch (SP) test, a miniaturised testing method, can offer a pragmatic alternative in the initial stages of development and understanding. SP testing can be used in tensile, fracture, fatigue and creep arrangements and has recently transitioned into a European Norm standard. Additionally, the miniaturised test method can enable the mechanical testing of as-built material which has too much residual stress for conventional specimen manufacture. The technique has been applied across various material systems and manufacturing methods including steels [11], AM nickel based superalloys [12] and weldments [13] and has been successfully employed for material ranking and material property estimation.

This research investigates the microstructure and high temperature mechanical properties of DSS 2205 manufactured via LPBF in as-built and heat-treated conditions, expanding upon the current literature [10,14–16]. High temperature SP testing (up to 750 °C) has been conducted with mechanical property estimations determined through comparison with a series of uniaxial tensile tests up to 300 °C. Microstructural assessment through EBSD analysis has been carried out to determine austenite/ferrite phase distributions and texture to establish its influence on performance across the range of temperatures studied.

2. Material and methods

2.1. Powder, LPBF, and heat treatment

Commercial DSS 2205 gas atomised powder was used in this research with a particle size distribution ($d_{10} - d_{90}$) of 15–45 μm. The as-supplied chemical composition (in wt%) was: 22.4 Cr, 5.17 Ni, 3.11 Mo, 1.04 Mn, 0.75 Si, 0.17 N, 0.018C, 0.018 P, 0.015 O, 0.004 S with Fe balance.

In this research, round cylindrical specimens (Ø11 mm × 65 mm) were built in the vertical orientation and hexagonal prisms (11 mm × 65 mm) in the horizontal orientation, using an EOS M2xx machine (EOS GmbH, Krailling, Germany), as shown in Fig. 1a. These were then manufactured into either uniaxial tensile test pieces (Fig. 1b.), or in the case of several of the vertically built cylinders, turned down to Ø9.5 mm rods. The top end of the rods were then sectioned into ~800 μm thick discs (indicated in Fig. 1c.), from which SP test specimens were manufactured. The key LPBF process parameters are provided in Table 1, with manufacturing completed in an argon environment. The heat treatment performed in this work was a solution annealing heat treatment, with the as-built specimens held at 1040 °C for 2 h followed by quenching. This heat treatment schedule was chosen with the purpose of delivering the maximum austenitic fraction, and simultaneously avoiding detrimental secondary phases. LPBF builds were post processed in both the as-built (AB) or heat-treated (HT) condition for the SP test specimens and only in the HT condition for the uniaxial tensile tests due to the level of residual stress in the AB condition which caused challenges in conventional specimen manufacture.

Table 1
LPBF process parameters.

Parameter	Value	Parameter	Value	Parameter	Value
Power	195 W	Hatch spacing	100 μm	Beam offset	0.01 mm
Scan speed	900 mm/s	Build platform	100 °C	Stripe width	5.00 mm
Layer height	20 μm	Atmosphere	Argon	Stripes overlap	0.3 mm

2.2. Mechanical characterisation

A series of standard uniaxial tensile tests were performed at room temperature, 200 °C and 300 °C on the HT specimens in both orientations, in accordance to ASTM E21–17 [17]. In the context of this research, these tests were performed to define key mechanical properties including ultimate tensile strength (R_m) and uniform elongation (A_g) as a basis for comparisons with room temperature results from literature and SP correlations at higher temperatures.

SP testing was performed on the disc specimens sectioned from the vertical builds in the AB and HT condition. Tests were undertaken across a range of temperatures, from room temperature up to and including 750 °C, using a single displacement rate of 0.2 mm•min^{-1} using a Ø2.5 mm hemispherical punch. SP specimens were prepared from the Ø9.5 mm, ~800 μm thick discs through being progressively ground by finer silicon carbide abrasive papers to produce the required specimen thickness of 500 μm ± 5 μm with a 1200 grit finish. The SP specimen is clamped between an upper and lower die, with loading imparted onto the disc via the hemispherical punch. Deflection readings are recorded via a linear variable displacement transducer (LVDT), measuring deformation on the lower side of the specimen through a quartz rod which maintains contact throughout the test. For the elevated temperature SP testing, two *K*-type thermocouples are positioned close to the surface of the disc, located through drilled holes in the upper die, ensuring temperature is kept within ±0.25% of the specified test temperature. The constant displacement rate SP tests conducted in this study produce a load-displacement response. The procedure of the SP tests

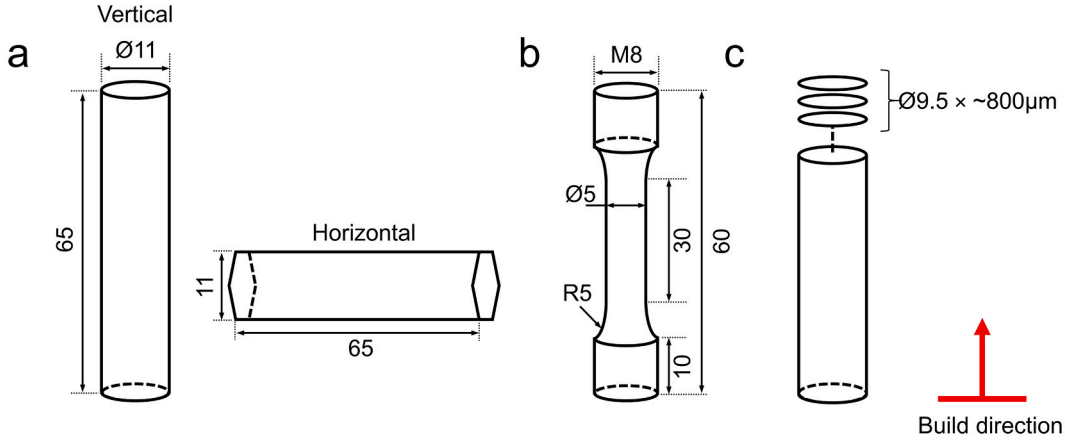

Fig. 1. Schematic of LPBF as-built and manufactured test specimen dimensions: **(a)** vertical specimens were built as cylinders and horizontal specimens built as hexagonal prisms, **(b)** uniaxial tensile test specimens manufactured from the heat-treated condition for both orientations and **(c)** discs sectioned from the top of vertically built cylinders from both as-built and heat-treated condition ahead of final preparation into small punch test specimens (Ø9.5 mm, 500 ± 5 μm). All dimensions in mm.

were carried out in accordance with the EN 10371 standard [18], except for using a specimen diameter of 9.5 mm. A schematic of the test arrangement is shown in Fig. 2.

2.3. Microstructural characterisation and fractography

Microstructural characterisation was performed post-test on the undeformed regions of fractured SP discs. These regions were sectioned and mounted to analyse both the AB and HT conditions across two orientations; the build direction (Z plane) and build direction plane (X-Y plane). Specimens were etched using Carpenter's reagent for 10s. Optical microscopy was performed using a Zeiss Primotech microscope. Electron Backscatter Diffraction (EBSD) and fractographic analysis was conducted on a Hitachi SU3500 Scanning Electron Microscope (SEM) operated at 20 kV. EBSD scans were conducted with a 0.25 μm step size at ×500 magnification across an approximate area of 275 μm × 200 μm and analysed using Oxford Instruments AZtec software. Deformed, substructured and recrystallized grains were identified by measuring the misorientation distribution and calculated using the recrystallization fraction function in HKL Channel 5. If the critical internal misorientation angle (θ_c) was less or greater than 2° then the grains were classified as fully recrystallized (RC) and deformed respectively. If a grain was composed of subgrains with internal misorientations of under 2° but the misorientation from subgrain to subgrain was above 2°, then the grain was classified as a substructured [19,20].

3. Results and discussion

3.1. Microstructure

Fig. 3 presents the optical micrographs of the AB and HT specimens in the unetched condition (Fig. 3a, d), the build plane (Fig. 3b, e) and the build direction (Fig. 3c, f). The unetched micrographs indicate the level of porosity in the AB and HT materials, with typical defects circled. Image analysis of a series of three unetched 2D sections in both the AB and HT condition revealed an average density of 99.96%, which corresponds well with previous studies on LPBF DSS 2205 [10,15]. The micrographs of the AB specimens (Fig. 3b, c) show the microstructure is dominated by ferrite. This phenomena occurs due to the molten powder solidifying as delta ferrite coupled with the rapid cooling rates in the LPBF process [21]. In the build direction, the AB specimens exhibit a columnar grain structure with a more equiaxed type structure on the orthogonal face in the build plane. The melt pool boundaries are somewhat visible in the AB specimens, indicated by white arrows, which helps to reveal two features in the AB microstructure. Firstly, the elongated grains in the build direction extend over several melt pools, revealing the epitaxial growth mechanism which occurs due to the remelting and solidification of previously deposited layers. Secondly, in the AB build plane, there is evidence of finer grains on the overlap of the melt pool boundaries. The micrographs of the HT specimens (Fig. 3e, f) show that the HT schedule has resulted in a significant increase in the austenite fraction, which arises due to the formation and movement of high angle grain boundaries at the solution annealing temperature [10]. The formed austenite can generally be divided into three groups; (i) formed along the melt pool boundaries during the process and grown during HT, (ii) needle-like laths and (iii) small islands of intragranular secondly austenite [14], indicated by the red, yellow and black arrows respectively in Fig. 3f.

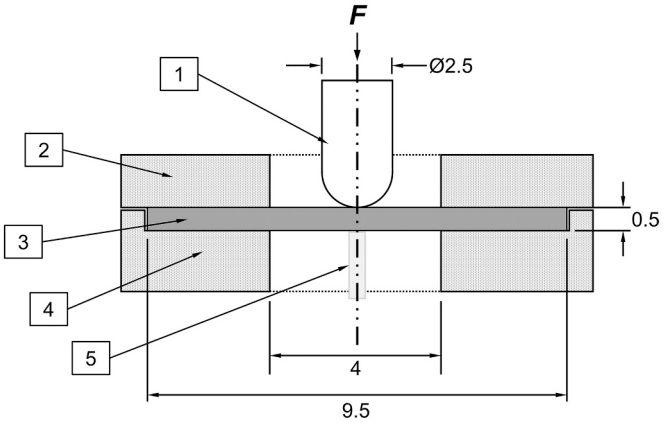

Fig. 2. Schematic of SP test arrangement (1. Hemispherical punch, 2. Upper die, 3. SP specimen 4. Lower die, 5. Quartz rod). All dimensions in mm.

Fig. 4 illustrates the phase distributions of the LPBF DSS 2205 microstructures of AB (Fig. 4a, b) and HT (Fig. 4c, d) specimens in both the build plane and build direction. A series of EBSD scans were performed across the AB and HT specimens to reliably determine the phase distribution of ferrite and austenite, and the percentage of recrystallisation present in the microstructures are reported in Table 2.

The phase maps of the AB specimens reveal >99% vol% ferrite which agrees with studies on AM DSS. The solution annealed heat treatment developed a dual phase microstructure with 53.4% Ferrite and 46.6% Austenite (Fig. 4c, d). The solution anneal also increased the fraction of fully recrystallized bcc Ferrite from 13.3% to 47.2% and reduced the sub-structured grain proportions from 86.7% to 51.7%, demonstrating that the heat treatment provided sufficient driving force for recrystallization. The recrystallisation fractions for both the bcc-ferrite and fcc-austenite are similar in the heat treated condition.

Fig. 5 shows the IPF maps and *Z*-IPFs of the bcc-ferrite (and fcc-austenite phase for the HT specimens) for the corresponding phase maps presented in Fig. 3. As is typical for the microstructures of steels solidified in a strong temperature gradient, such as that seen in LPBF, a pronounced crystallographic ⟨001⟩ texture of the ferrite phase in the AB condition is observed (Fig. 5a, b). In the HT condition (Fig. 5c, d), the texture in the ferrite phase is still present, although significantly reduced, due to the solution annealing which sees the introduction of austenite due to the formation and motion of high angle grain boundaries. The fcc-austenite phase in the HT condition is revealed to have a primarily preferred ⟨011⟩ texture, whereas the bcc-ferrite retains its preferred <001> texture (Fig. 5c, d). These texture preferences seen in the AB and HT condition in the build direction are consistent with other investigations on LPBF DSS 2205 [15,16]. The texture relationship of bcc ⟨001⟩//fcc<011> between the ferrite and austenite phases respectively, is a frequently reported relationship between fcc and bcc systems [22] and is equivalent to the Nishiyama–Wassermann (N–W) α ⟨011⟩//γ ⟨112⟩ orientation relationship previously reported [23,24].

3.2. Uniaxial tensile properties

Table 3 presents the tensile properties for the heat-treated LPBF DSS 2205 material in both the vertical and horizontal orientations across the three tested temperatures. The table provides the number of tests conducted and the average and standard deviation values for proof stress ($R_{0.2}$), ultimate tensile strength (R_m), uniform elongation (A_g) and elongation to fracture (A_f).

Fig. 6 graphically illustrates the influence of temperature on the uniaxial properties of the heat-treated specimens across the two build orientations. The horizontally oriented specimens exhibit an average increase of 10% across the three tested temperatures for $R_{0.2}$ and R_m, and a decrease in both A_g and A_f (between 9 and 30%, depending on test temperature and elongation type) compared to the vertically oriented specimens. An increase in strength coupled with a drop in ductility between the different orientations is commonplace in AM metallic materials due to the epitaxial grain growth that occurs as a result of the successive re-melting of layers during the LPBF process and the resulting thermal gradients in the build direction [7]. The influence of build orientation and temperature shown here has also been observed in investigations into tensile properties of LPBF austenitic stainless steels

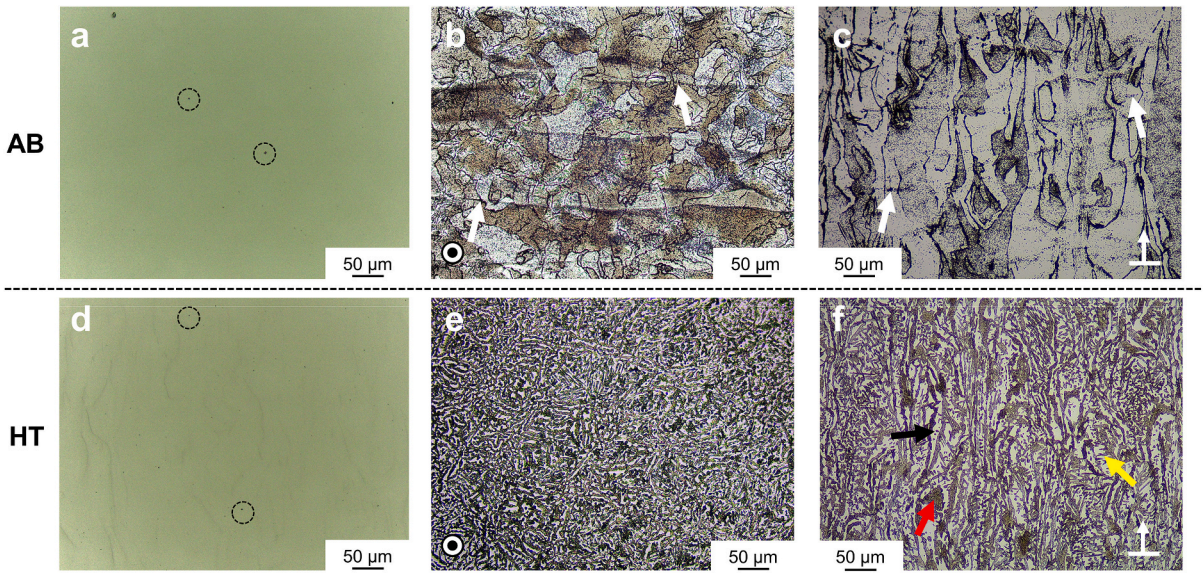

Fig. 3. Optical micrographs of LPBF DSS 2205 taken from **(a)** AB unetched **(b)** AB build plane **(c)** AB build direction **(d)** HT unetched **(e)** HT build plane and **(f)** HT build direction.

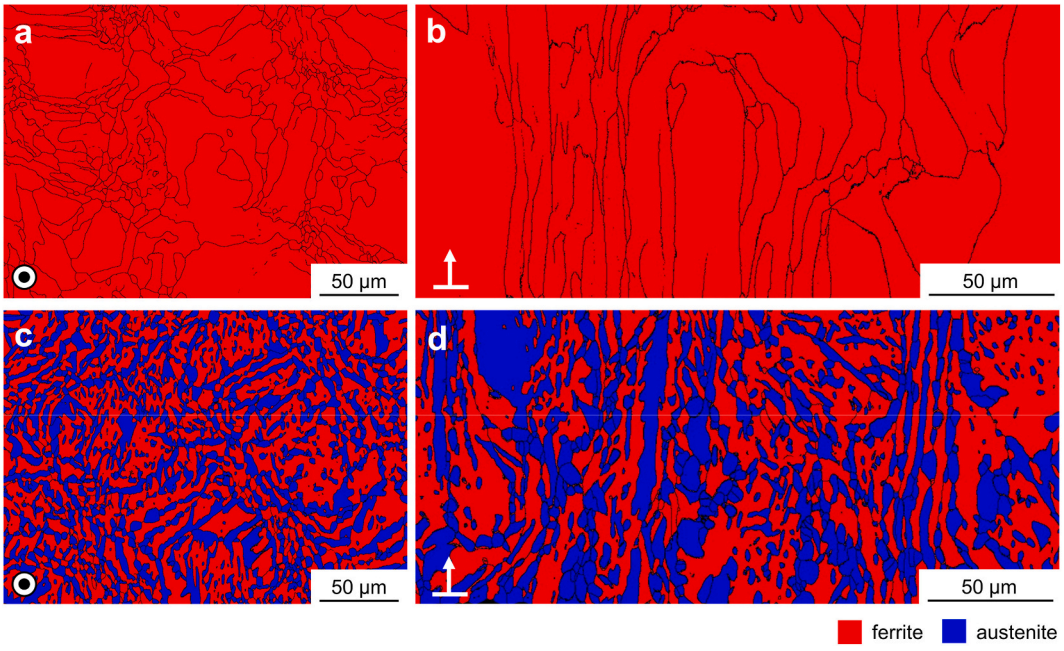

Fig. 4. Phase maps of LPBF DSS 2205 taken from **(a)** AB build plane **(b)** AB build direction **(c)** HT build plane and **(d)** HT build direction (grain boundaries determined by misorientation of 5°).

Table 2
Average proportion of ferrite and austenite phases, and recrystallisation fractions in LPBF DSS 2205 from AB and HT build plane Fig. 4 (a) and (c).

Material condition	Avg. phase (%)		Recrystallisation fraction (%)					
	Ferrite (BCC)	Austenite (FCC)	Ferrite (BCC)			Austenite (FCC)		
			RC	Sub-structured	Deformed	RC	Sub-structured	Deformed
As built	100.0	0.03	13.3	86.7	0.02	N/A	N/A	N/A
Heat treated	53.4	46.6	47.2	51.7	1.06	59.3	40.4	0.28

304 L [25] and 316 L [26,27]. The reduction in properties observed at 200 and 300 °C and the associated reduction factors, lie within ~10% for $R_{0.2}$ and R_m and ~ 20% for A_g and A_f when compared to those determined in the literature for the same or equivalent DSS alloy in sheet and bar form [28,29].

To understand how the tensile properties from this research corroborate with previous studies into LPBF DSS2205, a comparison of the room temperature tensile properties, R_m and A_g, has been conducted

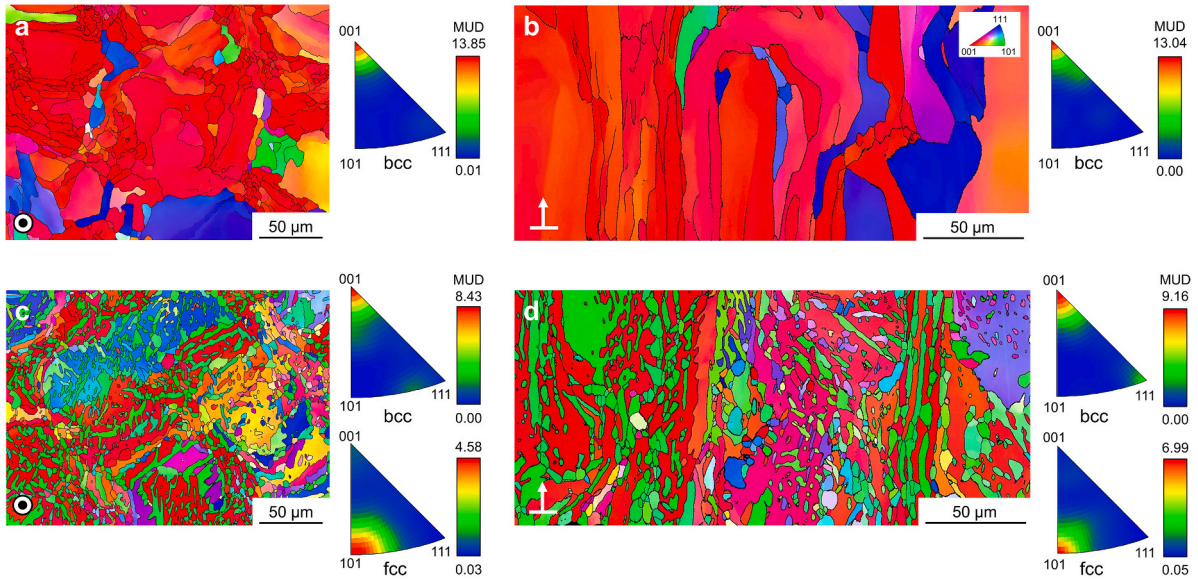

Fig. 5. IPF and *Z*-IPF maps of LPBF DSS 2205 taken from **(a)** AB build plane **(b)** AB build direction **(c)** HT build plane and **(d)** HT build direction.

Table 3
Average values and standard deviation of the measured properties from uniaxial tensile tests on heat-treated specimens.

Orientation	Number of tests	Temperature	$R_{0.2}$	R_m	A_g	A_f
		°C	MPa	MPa	%	%
Vertical	6	RT	482 ± 7	753 ± 8	29.7 ± 1.6	52.1 ± 2.7
	3	200	352 ± 5	624 ± 3	25.9 ± 0.8	37.9 ± 1.9
	5	300	347 ± 11	643 ± 7	23.7 ± 2.5	32.5 ± 5.0
Horizontal	5	RT	523 ± 6	832 ± 6	23.7 ± 0.7	36.9 ± 2.2
	4	200	392 ± 6	685 ± 6	21.9 ± 0.5	30.8 ± 1.8
	6	300	383 ± 3	697 ± 7	21.6 ± 0.8	28.4 ± 1.8

with the available literature, accounting for the individually published process parameter sets. This provides an insight into the apparent influence of process parameters on the tensile properties of LPBF DSS 2205 at room temperature. Figs. 7 and 8 demonstrate the relationship between R_m and A_g against laser power (Fig. 7a, 8a), scan speed (Fig. 7b, 8b) and laser energy (Fig. 7c, 8c), where laser energy, ψ, has been determined through (1) where P is laser power, v is scan speed, h is hatch spacing and d is layer height:

$$\psi = \frac{P}{v \bullet h \bullet d} \tag{1}$$

Whether data is taken from the AB or HT conditions is indicated by hollow and shaded data points respectively, with the various heat treatment regimens provided. The results obtained from literature are for vertically built LPBF DSS 2205 specimens only, and as a result, the second order polynomial trendlines and associated R^2 values for the heat-treated conditions do not include the horizontal build results from this study. The chosen trendline type comes from the knowledge that during LPBF at the extremes of laser energy input, defects can become prominent, such as lack of fusion which may occur at lower laser energy input values or keyhole porosity which can occur at very high laser energies [7,30]. Scatter of the results from literature has been provided where available and represents either standard deviation or range depending on the individual study, with relevant details found in [10,14–16].

The room temperature properties of the HT condition derived in this study sit well with previous investigations of LPBF DSS 2205. The R_m values of the vertically orientated specimens fall within ±12% when compared to the published literature, with the most significant difference seen in uniform elongation with an average increase of ~25%. While absolute trends between tensile properties and process parameters of LPBF DSS 2205 are difficult to determine here due to the wide

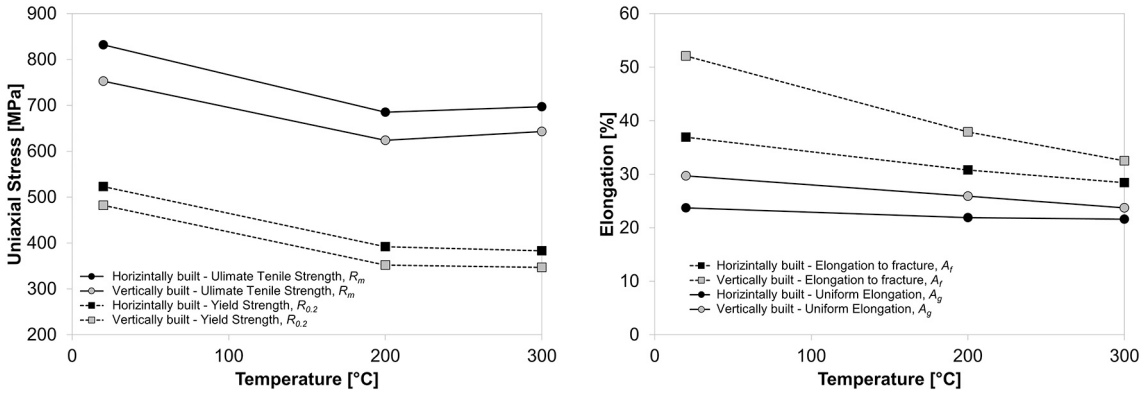

Fig. 6. Relationship of uniaxial properties vs. temperature for heat treated LPBF DSS2205 across two build orientations **(a)** $R_{0.2}$ and R_m **(b)** A_g and A_f.

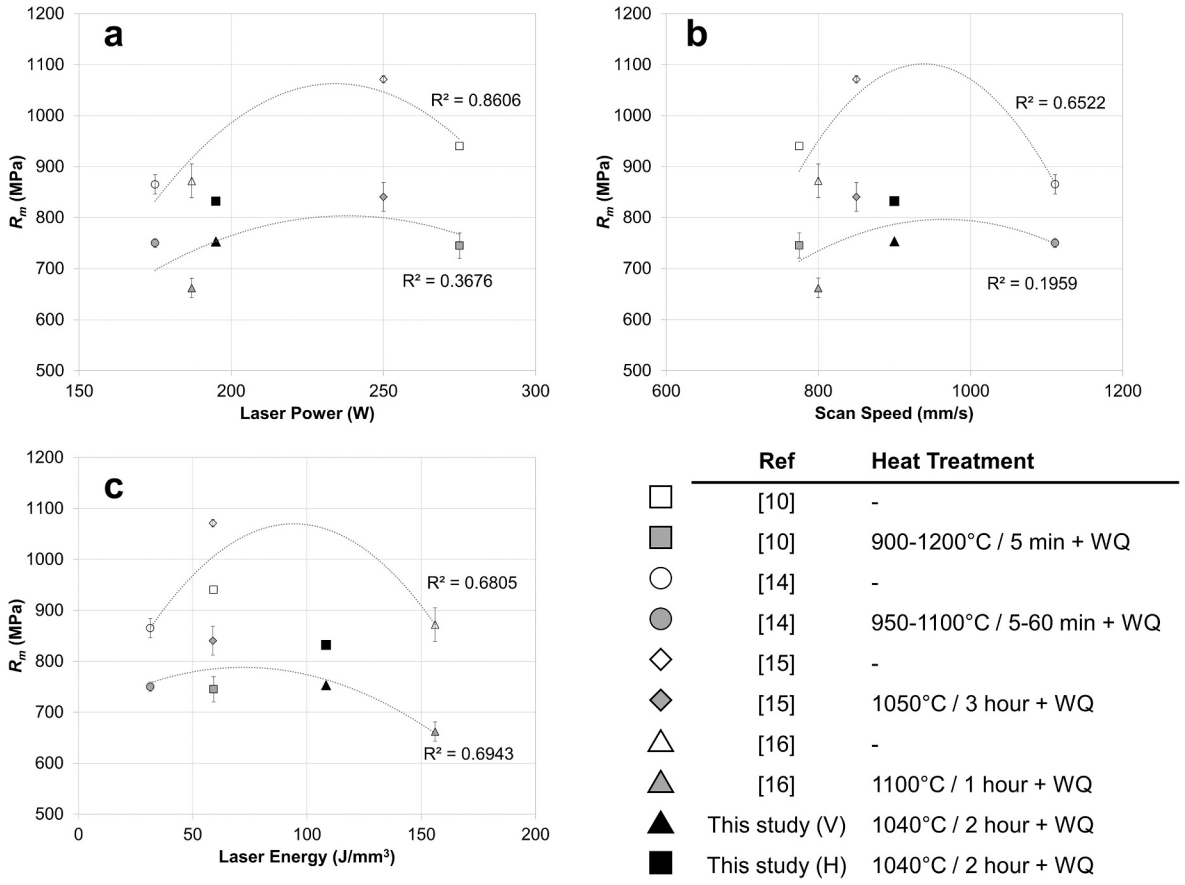

Fig. 7. LPBF DSS 2205 ultimate tensile strength against key process parameters **(a)** laser power **(b)** scan speed and **(c)** laser energy. Including data obtained from this study and available literature [10,14–16].

variety of process parameter combinations available, Figs. 7 and 8 do indicate trends that are commensurate to those seen in the literature [31].

3.3. SP testing

The load-displacement response for all the SP tests across the various temperatures is shown in Fig. 9, with the AB results provided in Fig. 9a. and the HT results in Fig. 9b. The response shown is characteristic of SP testing and can be split into different deformation regions, specifically elastic bending, plastic bending, membrane stretching and plastic instability, as reported in [32]. Key characteristics of the load-displacement curve include the peak load, F_{max}, and displacement at peak load, u_m, with these values often used in correlating with uniaxial tensile properties of R_m and A_g respectively.

The SP room temperature results follow the same trend observed in the literature and the uniaxial tensile results from this study, with the AB specimens exhibiting a higher strength (F_{max}) and reduced ductility (u_m) in comparison to the HT specimens. Similarly, the high temperature SP test results, up to 300 °C, also align with the high temperature uniaxial test results in this study, with reduced strength and ductility observed as test temperature increases. The increase in grain boundary density in the HT condition, as indicated in Figs. 3–5, is considered a key contributor to the increase of F_m seen in SP testing in the lower temperature range (<600 °C). Above this temperature, precipitates such as the σ phase can begin to form [33] with an increased driving force for these formations present in the HT condition due to nucleation predominantly occurring in ferrite-ferrite and ferrite-austenite grain boundaries, growing into the adjacent ferrite grains [34]. As a result, the AB condition sees a slight increase in F_m in comparison to the HT material at the two highest test temperatures.

Fig. 10 presents the key SP test values of F_{max} (Fig. 10a) and u_m (Fig. 10b) in the AB and HT condition over the tested temperature range. A third order polynomial trendline has been fitted to the F_{max} against temperature plot as this is akin to the trend in R_m across this temperature range in DSS 2205 sheet material [29]. A steady reduction in u_m is observed in the AB condition up until 500 °C, after which an increase in u_m occurs. This increase is attributed to the fully ferritic microstructure present in the AB condition. The ferritic bcc structure has a relatively high stacking fault energy [35], meaning that during the hot deformation of the SP test, dislocations can cross-slip and climb easily. As a result, dynamic recovery dominates the softening process, which is seen by the particularly slow increase in force during the early stages and throughout the SP test for the AB condition at 600 and 750 °C. For the HT condition, where the duplex microstructure is present, u_m is considered relatively stable with the load-displacement curves consistent in their appearance across the tested temperature range, although evidence of softening is starting to appear in the 750 °C result. An increase in fracture strain, albeit under uniaxial loading, of similar DSS materials at higher temperatures (>800 °C) has previously been reported [28]. These same trends are observed overall for high temperature (up to 700 °C) tensile properties of LPBF 316 L [26].

To determine correlated uniaxial properties from the SP tests, an empirical approach can be employed. Eqs. (2) and (3) show the typical equations used to correlate F_{max} to R_m and u_m to A_g respectively. Here t, is the specimen thickness and β_1, β_2, γ_1 and γ_2 are constants derived using linear regression from a series of SP and uniaxial data sets. Previous research has determined a wide range of values for β_i and γ_i depending on the material systems under investigation [32,36–38].

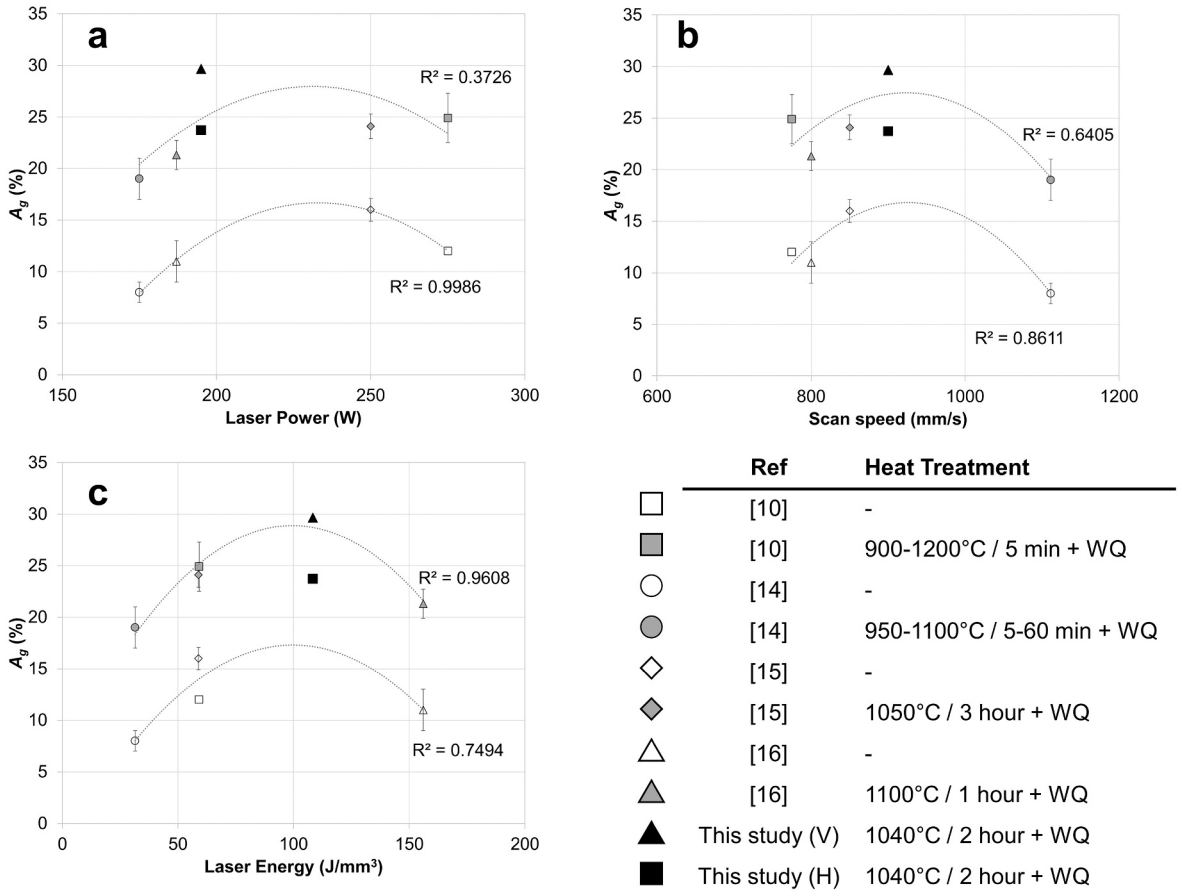

Fig. 8. LPBF DSS 2205 uniform elongation against key process parameters **(a)** laser power **(b)** scan speed and **(c)** laser energy. Including data obtained from this study and available literature [10,14–16].

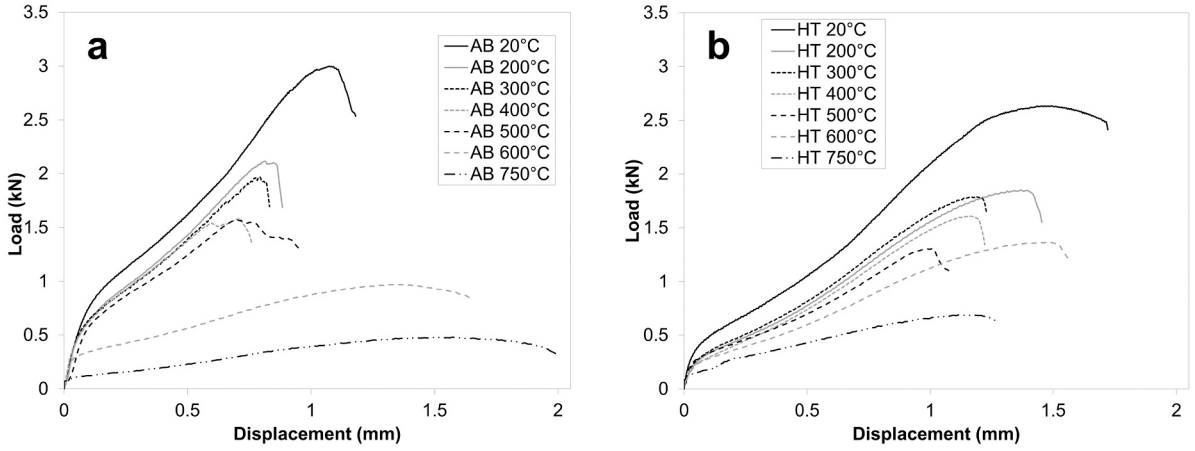

Fig. 9. SP load-displacement responses for LPBF DSS 2205 in the **(a)** as-built and **(b)** heat-treated conditions.

$$R_m = \beta_1 \bullet \frac{F_{max}}{u_m \bullet t} + \beta_2 \quad (2)$$

$$A_g = \gamma_1 \bullet u_m + \gamma_2 \quad (3)$$

Fig. 11 uses the limited available data sets to determine the correlation constant terms β_1, β_2, γ_1 and γ_2. Due to the biaxial tension stress state of SP testing, it is challenging for the SP test to account for any anisotropy that is present. Therefore, the SP results, which were manufactured from material sectioned from vertically built rods, have been correlated with the vertical uniaxial results since this will offer a conservative estimation of the high temperature properties.

Table 4 provides the predicted values of R_m and A_g for vertically built LPBF DSS 2205 based on the performed SP tests and using the derived Eqs. (4) and (5). These equations are revealed to deviate from larger SP studies on traditionally manufactured metallic materials [32,37]. Nonetheless, the individual data points from this research would sit within the scatter of these larger SP studies, which highlights that a universal SP to uniaxial property correlation, such as those using F_m and u_m, cannot be wholly independent of material properties [39], processing route and test temperature.

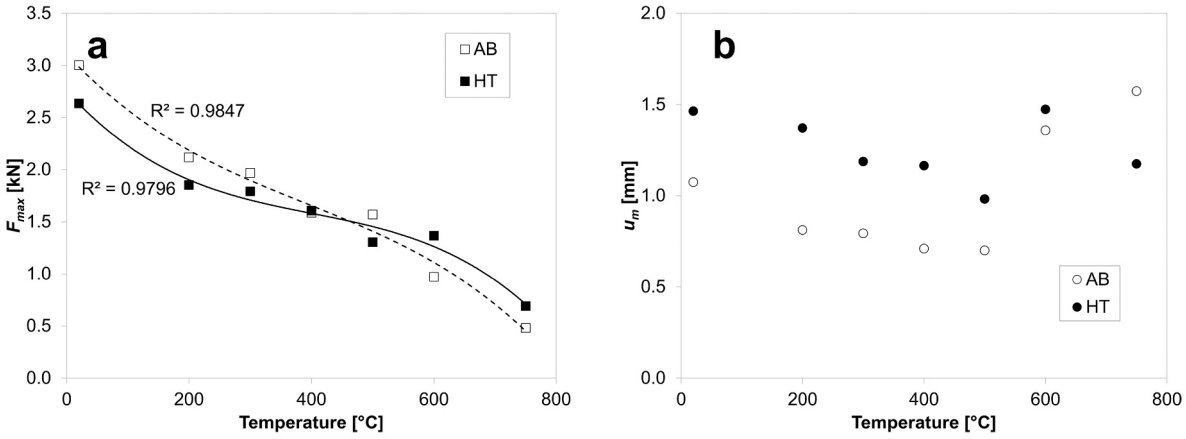

Fig. 10. Key characteristics obtained from SP testing for LPBF DSS 2205 in the as-built and heat-treated condition over the tested temperature range **(a)** F_{max} **(b)** u_m.

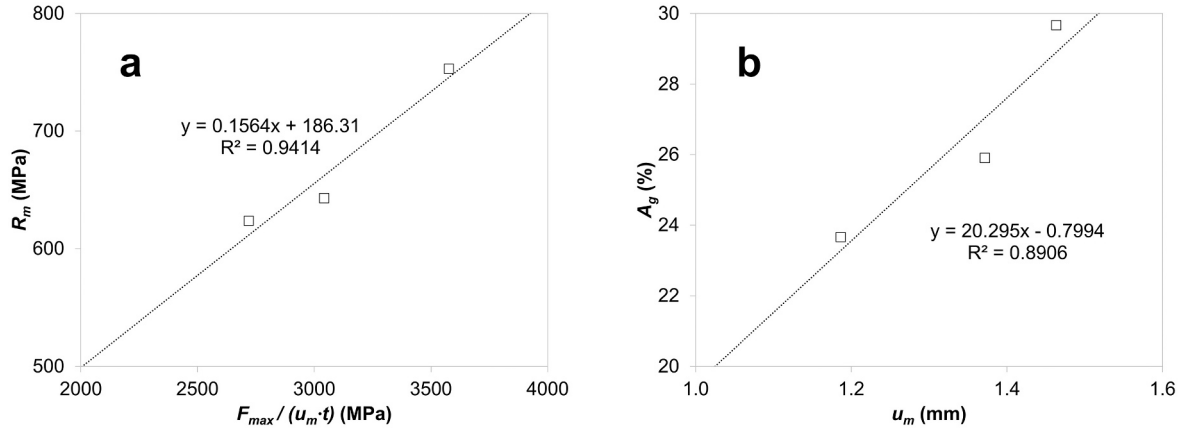

Fig. 11. SP to uniaxial correlations for LPBF DSS 2205 **(a)** R_m vs. $F_{max}/u_m \bullet t$ **(b)** A_g vs. u_m.

Table 4
Predicted values of R_m and A_g for LPBF DSS 2205 based on SP test results.

Temperature	As built		Heat treated	
°C	R_m (MPa)	A_g (%)	R_m (MPa)	A_g (%)
RT	1055	21.0	746	28.9
200	1009	15.7	612	27.0
300	962	15.3	662	23.3
400	881	13.6	618	22.8
500	885	13.4	602	19.1
600	408	26.8	476	29.1
700	282	31.1	370	23.0

$$R_m = 0.156 \bullet \frac{F_{max}}{u_m \bullet t} + 186.3 \quad (4)$$

$$A_g = 20.3 \bullet u_m - 0.80 \quad (5)$$

The predicted values based on Eqs. (4) and (5) reveal a decrease of 29% for R_m and an increase of 38% for A_g when comparing the AB to HT material at room temperature. These differences are comparable to that shown in the literature for LPBF DSS 2205 which reveals an average decrease in R_m of 20 ± 6% and an increase in A_g of 48 ± 15% between AB and HT material at room temperature [10,14–16], providing further evidence that SP testing offers an effective means of estimating mechanical properties for these materials.

The SP fracture surfaces presented in Fig. 12 illustrate that no discernible difference can be seen in the two contrasting post manufacture conditions and the two extreme temperatures. In all instances, a dominant circumferential crack is visible, along with dimpling emanating from the receiving hole, which are considered evidence of a predominantly ductile mode of failure. The final fracture for the room temperature as-built specimen (Fig. 12a) shows damage progressing from the circumference towards the centre, which corresponds well with this specimen displaying the largest load drop after it reaches F_m (Fig. 12a).

4. Conclusions

The microstructural characteristics and tensile behaviour of LPBF DSS 2205 has been investigated. Results have been generated on alternative orientations, in both as-built and heat-treated conditions, across a series of temperatures. Properties have been determined using conventional tensile testing up to 300 °C, whilst small punch (SP) testing was employed to predict higher temperature tensile results up to 750 °C. From this research, the following conclusions can be drawn:

- The as-built microstructure has been shown to be fully ferritic (>99.9%) with a strong <001> texture of the ferrite grains evident in both the build plane and build direction, as expected due to solidification taking place over the temperature gradient that occurs during the LPBF process.
- The phase distribution volume percentage was significantly modified through a solution annealing heat treatment, which lead to the desired dual phase microstructure, with the volume fraction of austenite increasing from a negligible presence to an average of 46.6%. The recrystallized microstructure shows a retained but

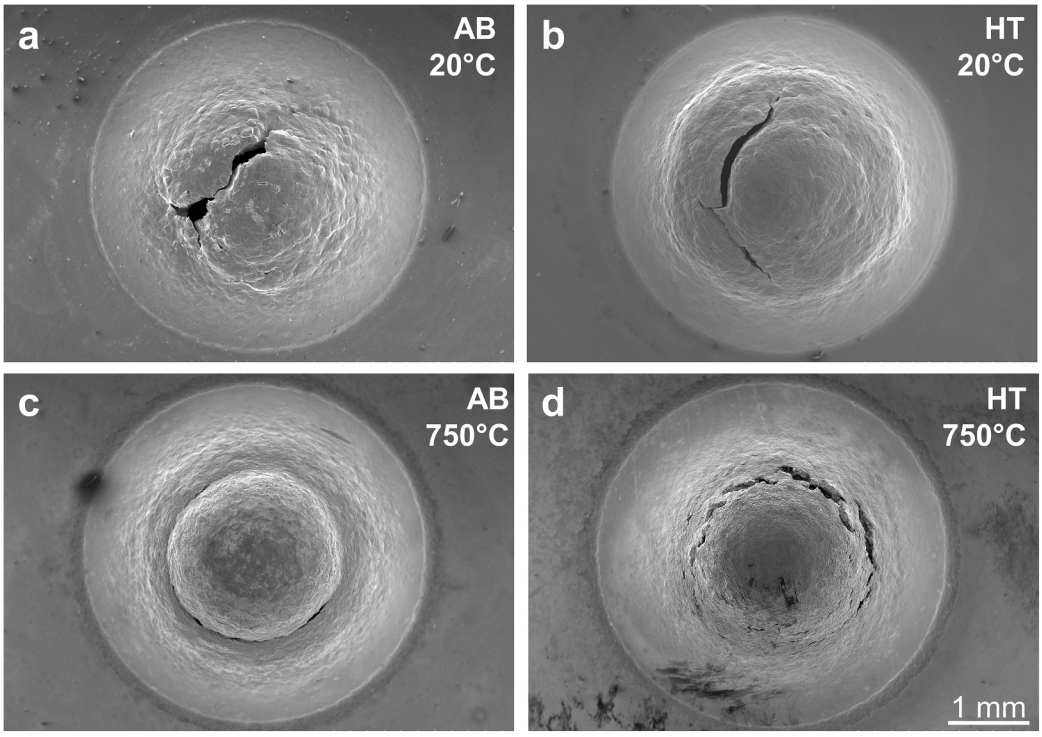

Fig. 12. Fracture surfaces of SP tested LPBF DSS 2205 in both as-built and heat-treated conditions, at 20 and 750 °C.

reduced <001> texture of ferrite while the formed austenite phase exhibits a < 011> texture preference.

- Epitaxial grain growth is revealed in the build direction due to the successive re-melting of layers that occurs during the LPBF process. The epitaxial structure is retained in the heat-treated condition where anisotropic properties are determined up to 300 °C. Consequently, the vertically built specimens show an increased strength and reduced ductility compared to the horizontally built specimens.
- Estimated properties generated through SP testing have successfully been correlated to the uniaxial high temperature mechanical properties of LPBF DSS 2205 in the as-built and heat-treated conditions, with trends commensurate with that seen in the literature for traditional manufactured DSS 2205. This includes an ever-decreasing ultimate tensile strength (R_m) with increasing temperature, and ductility values that steadily decrease with temperature but then rising beyond 600 °C due to dynamic recovery during hot deformation.

Data availability

The raw/processed data required to reproduce these findings cannot be shared at this time as the data also forms part of an ongoing study.

Declaration of Competing Interest

The authors declare that they have no known competing financial interests or personal relationships that could have appeared to influence the work reported in this paper.

Acknowledgements

The current research was funded under the EPSRC Industrial Case Award EP/T517537/1. The provision of a research bursary, materials and supporting information from Rolls-Royce plc. is gratefully acknowledged.

References

[1] R.M. Davison, J.D. Redmond, A guide to using duplex stainless steels, Mater. Des. 12 (4) (1991) 187–192, https://doi.org/10.1016/0261-3069(91)90162-W.
[2] J.R. Davies, ASM Specialty Handbook: Stainless Steels, ASM International, 1994.
[3] R. Gunn, Duplex Stainless Steels: Microstructure, Properties and Applications, Woodhead Publishing Ltd, 1997.
[4] K.H. Lo, C.H. Shek, J.K.L. Lai, Recent developments in stainless steels, Mater. Sci. Eng. R. Rep. 65 (4–6) (2009) 39–104, https://doi.org/10.1016/j.mser.2009.03.001.
[5] S.J. Zinkle, G.S. Was, Materials challenges in nuclear energy, Acta Mater. 61 (3) (2013) 735–758, https://doi.org/10.1016/j.actamat.2012.11.004.
[6] H.D. Solomon, T.M. Devine Jr., Duplex stainless steels - a tale of two phases, in: Duplex Stainless Steels, 1982, pp. 693–756.
[7] T. DebRoy, et al., Additive manufacturing of metallic components – process, structure and properties, Prog. Mater. Sci. (2018), https://doi.org/10.1016/j.pmatsci.2017.10.001.
[8] P. Bajaj, A. Hariharan, A. Kini, P. Kürnsteiner, D. Raabe, E.A. Jägle, Steels in additive manufacturing: a review of their microstructure and properties, Mater. Sci. Eng. A 772 (October) (2019) 2020, https://doi.org/10.1016/j.msea.2019.138633.
[9] N. Haghdadi, M. Laleh, M. Moyle, S. Primig, Additive manufacturing of steels: a review of achievements and challenges, J. Mater. Sci. 56 (1) (2021) 64–107, https://doi.org/10.1007/s10853-020-05109-0.
[10] F. Hengsbach, et al., Duplex stainless steel fabricated by selective laser melting - microstructural and mechanical properties, Mater. Des. 133 (2017) 136–142, https://doi.org/10.1016/j.matdes.2017.07.046.
[11] T.E. García, C. Rodríguez, F.J. Belzunce, C. Suárez, Estimation of the mechanical properties of metallic materials by means of the small punch test, J. Alloys Compd. 582 (Jan. 2014) 708–717, https://doi.org/10.1016/j.jallcom.2013.08.009.
[12] S.J. Davies, S.P. Jeffs, M.P. Coleman, R.J. Lancaster, Effects of heat treatment on microstructure and creep properties of a laser powder bed fused nickel superalloy, Mater. Des. 159 (Dec. 2018) 39–46, https://doi.org/10.1016/J.MATDES.2018.08.039.
[13] Y. Fan, B.L. Yang, T.G. Liu, Y.H. Lu, Effect of inhomogeneous microstructure on the deformation and fracture mechanisms of 316LN stainless steel multi-pass weld joint using small punch test, J. Nucl. Mater. 538 (2020), 152239, https://doi.org/10.1016/j.jnucmat.2020.152239.
[14] J. Kunz, A. Boontanom, S. Herzog, P. Suwanpinij, A. Kaletsch, C. Broeckmann, Influence of hot isostatic pressing post-treatment on the microstructure and mechanical behavior of standard and super duplex stainless steel produced by laser powder bed fusion, Mater. Sci. Eng. A 794 (February) (2020) 139806, https://doi.org/10.1016/j.msea.2020.139806.
[15] S. Papula, et al., Selective laser melting of duplex stainless steel 2205: effect of post-processing heat treatment on microstructure, mechanical properties, and corrosion resistance, Materials (Basel). 12 (15) (2019) 1–15, https://doi.org/10.3390/ma12152468.

[16] G.N. Nigon, O. Burkan Isgor, S. Pasebani, The effect of annealing on the selective laser melting of 2205 duplex stainless steel: microstructure, grain orientation, and manufacturing challenges, Opt. Laser Technol. 134 (September 2020) (2021) 106643, https://doi.org/10.1016/j.optlastec.2020.106643.
[17] ASTMv, Standard Test Methods for Elevated Temperature Tension Tests of Metallic Materials, ASTM International: West Conshohocken, 2017.
[18] EN 10371:2021, Metallic Materials - Small Punch Test Method, 2021.
[19] P.J.P. Kañetas, J. Calvo, P. Rodriguez-Calvillo, J.M.C. Marrero, M.A.Z. Antuñano, M.P. Guerrero-Mata, Ebsd study of delta-processed ni-based superalloy, Metals (Basel). 10 (11) (2020) 1–14, https://doi.org/10.3390/met10111466.
[20] B.R. Chen, A.C. Yeh, J.W. Yeh, Effect of one-step recrystallization on the grain boundary evolution of CoCrFeMnNi high entropy alloy and its subsystems, Sci. Rep. 6 (February) (2016) 1–9, https://doi.org/10.1038/srep22306.
[21] K. Saeidi, L. Kevetkova, F. Lofaj, Z. Shen, Novel ferritic stainless steel formed by laser melting from duplex stainless steel powder with advanced mechanical properties and high ductility, Mater. Sci. Eng. A 665 (2016) 59–65, https://doi.org/10.1016/j.msea.2016.04.027.
[22] T.J. Headley, J.A. Brooks, A new Bcc-Fcc orientation relationship observed between ferrite and austenite in solidification structures of steels, Metall. Mater. Trans. A Phys. Metall. Mater. Sci. 33 (1) (2002) 5–15, https://doi.org/10.1007/s11661-002-0001-0.
[23] G. Wassermann, K. Mitt, About the mechanism of α–γ transformation of the iron, Wilh.-Inst. Eisenforsch 17 (1935) 149.
[24] Z. Nishiyama, X-ray investigation of the mechanism of the transformation from face centered cubic lattice to body centered cubic, Sci. Rep. Tohoku Univ. 23 (1934) 637.
[25] P. Kumar, Z. Zhu, S.M.L. Nai, R.L. Narayan, U. Ramamurty, Fracture toughness of 304L austenitic stainless steel produced by laser powder bed fusion, Scr. Mater. 202 (2021), 114002, https://doi.org/10.1016/j.scriptamat.2021.114002.
[26] S. Dryepondt, P. Nandwana, P. Fernandez-Zelaia, F. List, Microstructure and high temperature tensile properties of 316L fabricated by laser powder-bed fusion, Addit. Manuf. 37 (November 2020) (2021) 101723, https://doi.org/10.1016/j.addma.2020.101723.
[27] J. Suryawanshi, K.G. Prashanth, U. Ramamurty, Mechanical behavior of selective laser melted 316L stainless steel, Mater. Sci. Eng. A 696 (January) (2017) 113–121, https://doi.org/10.1016/j.msea.2017.04.058.
[28] L. Gardner, Y. Bu, P. Francis, N.R. Baddoo, K.A. Cashell, F. McCann, Elevated temperature material properties of stainless steel reinforcing bar, Constr. Build. Mater. 114 (2016) 977–997, https://doi.org/10.1016/j.conbuildmat.2016.04.009.
[29] L. Gardner, A. Insausti, K.T. Ng, M. Ashraf, Elevated temperature material properties of stainless steel alloys, J. Constr. Steel Res. 66 (5) (2010) 634–647, https://doi.org/10.1016/j.jcsr.2009.12.016.
[30] H. Fayazfar, et al., A critical review of powder-based additive manufacturing of ferrous alloys: process parameters, microstructure and mechanical properties, Mater. Des. 144 (2018) 98–128, https://doi.org/10.1016/j.matdes.2018.02.018.
[31] J.A. Cherry, H.M. Davies, S. Mehmood, N.P. Lavery, S.G.R. Brown, J. Sienz, Investigation into the effect of process parameters on microstructural and physical properties of 316L stainless steel parts by selective laser melting, Int. J. Adv. Manuf. Technol. 76 (5–8) (2015) 869–879, https://doi.org/10.1007/s00170-014-6297-2.
[32] J. Torres, A.P. Gordon, Mechanics of the Small Punch Test: A Review and Qualification of Additive Manufacturing Materials vol. 56, no. 18, Springer, US, 2021.
[33] I. Calliari, M. Pellizzari, M. Zanellato, E. Ramous, The phase stability in Cr-Ni and Cr-Mn duplex stainless steels, J. Mater. Sci. 46 (21) (2011) 6916–6924, https://doi.org/10.1007/s10853-011-5657-7.
[34] H. Sieurin, R. Sandström, Sigma phase precipitation in duplex stainless steel 2205, Mater. Sci. Eng. A 444 (1–2) (2007) 271–276, https://doi.org/10.1016/j.msea.2006.08.107.
[35] J.A. Yan, C.Y. Wang, S.Y. Wang, Generalized-stacking-fault energy and dislocation properties in bcc Fe: a first-principles study, Phys. Rev. B - Condens. Matter Mater. Phys. 70 (17) (2004) 1–5, https://doi.org/10.1103/PhysRevB.70.174105.
[36] S. Davies, S. Jeffs, R. Lancaster, G. Baxter, High temperature deformation mechanisms in a DLD nickel superalloy, Materials (Basel). 10 (5) (2017), https://doi.org/10.3390/ma10050457.
[37] N. Leclerc, A. Khosravani, S. Hashemi, D.B. Miracle, S.R. Kalidindi, Correlation of measured load-displacement curves in small punch tests with tensile stress-strain curves, Acta Mater. 204 (2021), 116501, https://doi.org/10.1016/j.actamat.2020.116501.
[38] R.J. Lancaster, S.P. Jeffs, B.J. Haigh, N.C. Barnard, Materials & design derivation of material properties using small punch and shear punch test methods, Mater. Des. 215 (2022), 110473, https://doi.org/10.1016/j.matdes.2022.110473.
[39] E. Altstadt, M. Houska, I. Simonovski, M. Bruchhausen, S. Holmström, R. Lacalle, On the estimation of ultimate tensile stress from small punch testing, Int. J. Mech. Sci. 136 (2018) 85–93, https://doi.org/10.1016/j.ijmecsci.2017.12.016.